International Journal of Minerals, Metallurgy and Materials
Volume 25, Number 12, December 2018, Page 1389
https://doi.org/10.1007/s12613-018-1693-5

Sintering study of Ti6Al4V powders with different particle sizes and their mechanical properties

José Luis Cabezas-Villa[1)], *José Lemus-Ruiz*[1)], *Didier Bouvard*[2)], *Omar Jiménez*[3)], *Héctor Javier Vergara-Hernández*[4)], *and Luis Olmos*[5)]

1) University Michoacana of San Nicolás of Hidalgo, IIMM, Morelia 58060, México
2) University Grenoble Alpes, CNRS, SIMaP, Grenoble 38000, France
3) University of Guadalajara, Departamento de Ingeniería de Proyectos, Zapopan 45100, México
4) National Technological Institute of Mexico, I. T. Morelia, Morelia 58120, México
5) University Michoacana of San Nicolás of Hidalgo, INICIT, Morelia 58060, México
(Received: 6 March 2018; revised: 19 June 2018; accepted: 21 June 2018)

Abstract: Ti6Al4V powders with three different particle size distributions (0–20, 20–45, and 45–75 μm) were used to evaluate the effect of the particle size distribution on the solid-state sintering and their mechanical properties. The sintering kinetics was determined by dilatometry at temperatures from 900 to 1260°C. The mechanical properties of the sintered samples were evaluated by microhardness and compression tests. The sintering kinetics indicated that the predominant mechanism depends on the relative density irrespective of the particle size used. The mechanical properties of the sintered samples are adversely affected by increasing pore volume fraction. The elastic Young's modulus and yield stress follow a power law function of the relative density. The fracture behavior after compression is linked to the neck size developed during sintering, exhibiting two different mechanisms of failure: interparticle neck breaking and intergranular cracking in samples with relative densities below and above of 90%, respectively. The main conclusion is that relative density is responsible for the kinetics, mechanical properties, and failure behavior of Ti6Al4V powders.

Keywords: Ti6Al4V powders; dilatometry; microhardness; sintering kinetics; compression; failure behavior

1. Introduction

Titanium and its alloys are relatively new engineering materials with high specific strength and lightness, excellent corrosion resistance, and exceptional biocompatibility [1]. The Ti6Al4V alloy is one of the most commonly used, including in aerospace [2–4] and biomedical applications such as in bone implants [5–6]. Over the past two decades, many jobs have been dedicated to researching the best method to manufacture Ti6Al4V by powder metallurgy (PM). Different PM techniques have been considered to produce dense and porous components made from this alloy [7–13]. To achieve complete densification, hot isostatic pressure, channel angular pressure, and spark plasma sintering have yielded the best results [11–13].

Recently, additive fabrication techniques such as electron beam melting (EBM) have produced metallic parts with a complex shape by melting successive layers of powders [14–17]. However, conventional PM methods, including powder pressing and pressureless solid-state sintering, remain the most pertinent route to producing different and complex components with controlled mechanical properties. The residual porosity after conventional sintering strongly reduces the mechanical properties of the sintered components, which can be beneficial in certain applications, especially bone implants.

Control of the porosity (shape, size, and volume fraction) is based on the knowledge of sintering parameters such as particle size, temperature, and sintering plateau because they play a fundamental role in the final densification [8,18–20]. Different studies have evaluated the effect of pressure and particle size on densification during compaction [21], and a

Corresponding author: Luis Olmos E-mail: luisra24@gmail.com

reduction of the particle size is known to accelerate the sintering and reduce the sintering activation temperature [22]. However, nanopowders are not easy to handle, especially in an industrial process. Thus, their price remains very high.

Xu and Nash [23] performed a dilatometric study of the Ti6Al4V powders sintered in vacuum at different heating rates, and they estimated the activation energy for the densification process. They found that densification is driven by the lattice diffusion mechanism. However, higher relative densities can also be achieved through sintering under flowing Ar [9,23–25]. They estimated a wide range of activation energy values (131–328 $kJ \cdot mol^{-1}$); however, they concluded that lattice diffusion is the predominant mechanism. Nonetheless, the effects of particle size and sintering temperature on the densification process as well as on the final properties of the sintered component from this alloy remain unclear. Thus, industrial applications remain limited.

Here, we investigate the effect of particle size, different thermal schedules, and initial packing on the sintering kinetics and mechanical properties of Ti6Al4V powders. The sintering kinetics were estimated from dilatometry tests. The microstructural features of sintered samples were observed by scanning electron microscopy (SEM), and the mechanical properties were evaluated by microhardness and compression tests. A failure analysis after compression testing enabled observation of cracks after compression, and the failure behavior was characterized as a function of relative density.

2. Experimental

Commercial Ti6Al4V alloy powders (Raymor, Quebec, Canada) with particle size distributions between 0 and 45 μm and 45–105 μm were used. The powders were sieved into three particle-size ranges based on the International Sieve Equivalency with the EE standard of ASTM International (ASTM E 11-87 [26]) using mesh equivalents of 200, 325, and 635. This process resulted in a nominal aperture in microns of 75, 45, and 20 μm, respectively. The shape and size of the different sieved powders were observed by SEM (JEOL JSM6400), as shown in Figs. 1(a)–1(c). In addition, the particle size distribution was measured via the laser light scattering technique (Coulter LS100Q). The three size distributions used in this work are shown in Fig. 1(d).

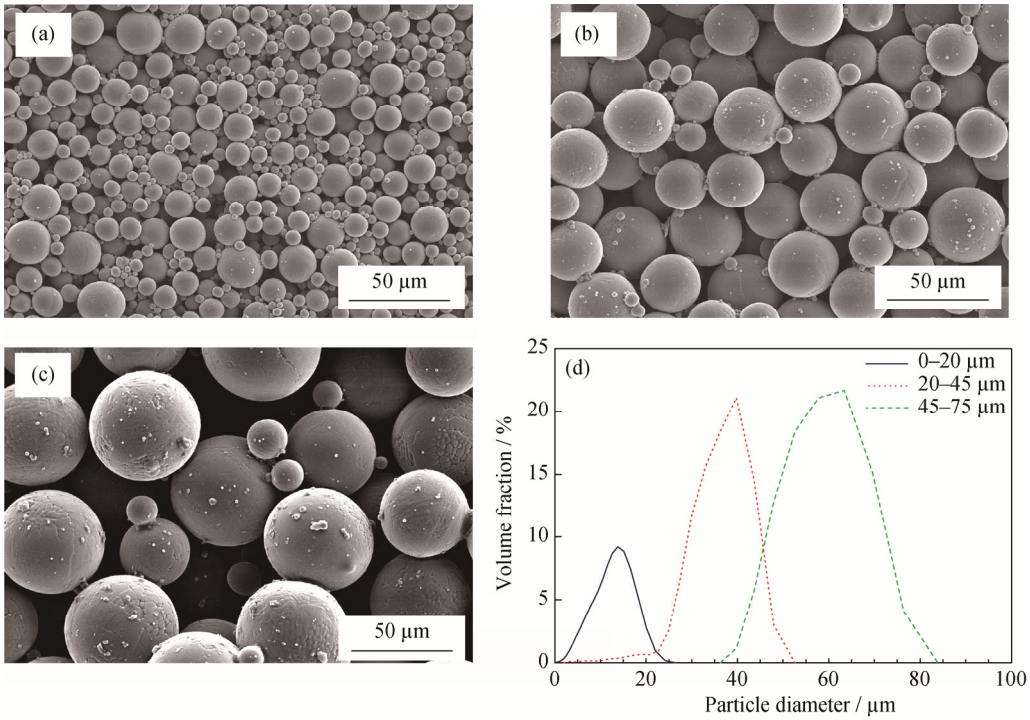

Fig. 1. SEM micrographs of sieved Ti6Al4V powders: (a) 0–20 μm, (b) 20–45 μm, and (c) 45–75 μm; (d) particle size distribution of the three ranges of particles.

Two approaches were used for the sintering study: sintering was evaluated (i) in the α-phase range of Ti at low temperatures between 900 and 1000°C and (ii) at elevated temperatures between 1150 and 1260°C after the transition of the Ti from the α to the β phase. In both cases, cylindrical compacts 8 mm in diameter and 10 mm in height were fabricated. Samples sintered at low temperatures were prepared by pouring powders into 8-mm-diameter

zirconia crucibles to obtain compacts with a 30% or higher volume fraction of pores. Compacts sintered at elevated temperatures were compacted in an 8-mm diameter steel die with a pressure of 500 MPa using a solution of polyvinyl alcohol (PVA) as a binder at 1wt%. The binder was subsequently removed by heat treatment at 500°C for 30 min under an argon atmosphere. The green density of these compacts was approximately 70%; the main goal of these samples was the formation of highly dense compacts.

Sintering experiments were performed on a Linseis L75V vertical dilatometer at 25°C·min^{-1} with a plateau of 1 h to assess the sintering kinetics. The dilatometer was purged with flowing high-purity argon for 30 min to remove the air before the sample was heated. After sintering, all samples were cut and metallographically prepared for SEM observation. The samples' microhardness was measured on cross-sectional polished surfaces via a microhardness tester (Mitutoyo MVK-HVL) with a load of 5 N and a dwell time of 15 s [27].

After sintering, the bottom and top surfaces of samples were polished, and simple compression tests were performed following ASTM D695-02 with an Instron 1150 universal mechanical testing machine at a strain rate of 0.5 mm·min^{-1} [28]. The elastic modulus (E) and the yield strength (σ_y) were estimated from the stress–strain curve obtained from the load-displacement data provided by the Instron universal machine. To calculate the stress, the surface area of the sample was corrected by assuming that the volume was constant during compression. This assumption is likely false—especially for the less dense samples; however, it is reasonable at low strain in the domain where E and σ_y are estimated. The axial strain is calculated as the ratio of the real axial displacement (after machine stiffness correction) to the initial height of samples. After compression tests, several micrographs of the fractured samples collected by SEM were used to analyze the origin and propagation of the fissures.

3. Results and discussion

3.1. Dilatometry analysis

The axial shrinkage as a function of the time throughout the sintering cycle for samples sintered at different temperatures or with different particle sizes at the same temperature are shown in Fig. 2. Initially, a positive deformation due to the thermal expansion of the samples is obvious. When sintering is activated, shrinkage is observed in the curve near 800°C for all samples. After that, pronounced shrinkage continues until the isothermal temperature is reached. Afterward, the shrinkage behaves exponentially until the sintering plateau is attained. Finally, the shrinkage, which is due to the sample cooling, is almost linear. Shrinkage increases with increasing temperature and with decreasing particle size, consistent with the sintering theory described by Bolzoni *et al.* [29].

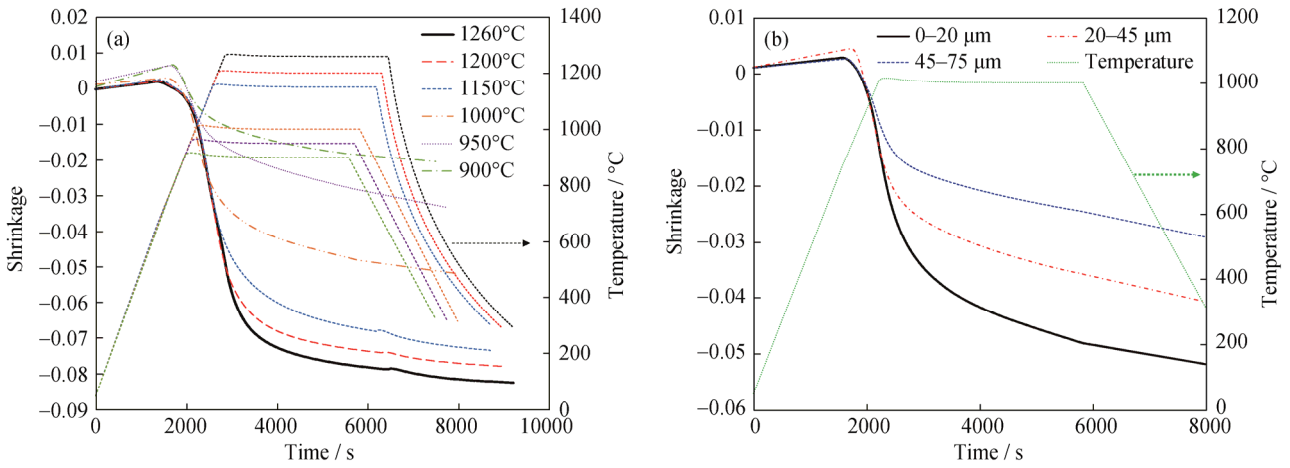

Fig. 2. Shrinkage as a function of time and temperature (a) at different temperatures for samples with particles sizes less than 20 μm and (b) at 1000°C for the three different particle size distributions.

To illustrate the effect of the sintering temperature, Fig. 2(a) shows the shrinkage as a function of time for the different temperatures used to sinter the sample, for samples with a particle size distribution of 0–20 μm. Shrinkage at higher temperatures was four-fold greater than that achieved at lower temperatures for the same powder sizes. The greater difference between the maximal shrinkage reached at 950°C and 1000°C is likely associated with

atomic mobility due to the crystalline structure of the α and β phases of the alloy because the phase-transition temperature is reported to be 980°C. However, the transition from α to β estimated from the dilatometry curves for all samples in this work is 1096°C. The increase in the β transus temperature could be associated with oxygen content because it is an α stabilizer. The transition temperature for Ti6Al4V has been reported to increase to 1034°C because of residual oxygen after sintering [30]. The oxygen content in the surface of the Ti6Al4V particles and the residual oxygen after PVA elimination could increase the oxygen content in the system, promoting stabilization of the α phase. Nevertheless, the oxygen content was not measured because such measurements are beyond the scope of the present work.

Fig. 2(b) shows the shrinkage as a function of time for samples sintered at 1000°C with three different particle sizes. Greater shrinkage is seen with finer powders—1.27 times greater than the shrinkage of intermediate powders and 1.73 times greater than that of coarser powders.

Fig. 3 shows the green and sintered relative densities as a function of the sintering temperature for different particle sizes. The green density of the samples sintered at lower temperatures is approximately 55% because of the initial particle packing being obtained by simply pouring the powders into a zirconia crucible. This procedure was used to fabricate compacts with a greater volume fraction of pores, thereby enabling the effect of the pores on the compacts' mechanical properties to be investigated. However, samples sintered at higher temperatures have green densities of 71%. These samples were obtained by uniaxial compression of powders at 500 MPa.

In order to compare the maximum sintered density as a function of the initial packing, one sample of each particle size was sintered at 1260°C (filled symbols in Fig. 3). The maximum density reached (96%) corresponds to the smaller particles sintered at the higher temperature after compression of powders. Nevertheless, the sample sintered at the same temperature but with a green density of 55% reached a relative density of 92.5%, which means that the initial packing only slightly influences the final density. Nevertheless, this difference in density strongly influences the mechanical properties, especially for structural applications, where demand higher relative densities. The densities of the sintered samples agree with those reported by Yan *et al.* [8], who evaluated three different particle sizes of Ti6Al4V alloy sintered at 1300°C under vacuum.

The highest sintered relative density (96%) value is 14% higher than that reported by Panigrahi *et al.* [31], who used irregularly shaped titanium powders (15 and 20 μm) sintered at 1250°C. However, this value is similar to that reported by Kim *et al.* [32], who determined a value of 95% for Ti6Al4V alloy samples sintered at 1360°C with a heating rate of 5°C·min^{-1} and a residence time of 120 min. For the intermediate particle size distribution, relative density values between 88% and 92% were obtained. For the coarser powders, the relative densities reached a range between 76% and 78% for samples sintered in the same temperature range.

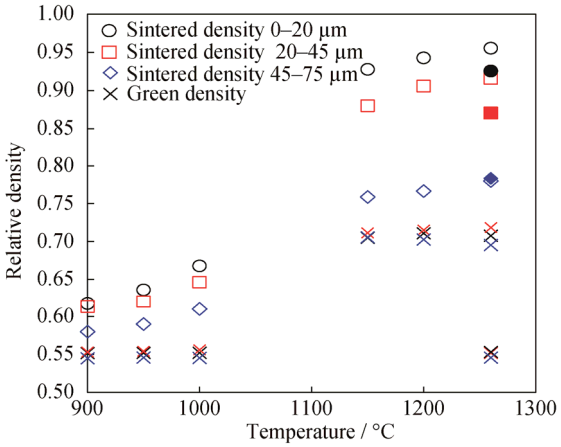

Fig. 3. Green and sintered relative densities as functions of the sintering temperature.

The densification rate of samples with a particle size less than 20 μm during the sintering plateau for different temperatures was plotted as a function of relative density (Fig. 4). Samples sintered at temperatures where the α phase is predominant are presented in Fig. 4(a); Fig. 4(b) presents temperatures where the β phase is predominant. For all of the samples, the maximum densification rate occurs at the beginning of the sintering plateau. It then decreases as the relative density increases. Notably, the relative density at the beginning of the sintering plateau increases with increasing temperature. To compare between samples, the same relative density is chosen. We estimated that the densification rate is slowed tenfold by reducing the sintering temperature from 1260 to 1150°C. This reduction is 13 times greater when the α phase is driving the sintering, i.e., at lower temperatures (Fig. 4(a)). The densification rate is higher for the β phase domain despite the relative density being approximately 80%; however, the densification rate is very similar for all samples at the end of the plateau, which suggests that the densification achieved during the sintering plateau reaches equilibrium, which further suggests that there is a maximum value of densification that can be achieved at each temperature.

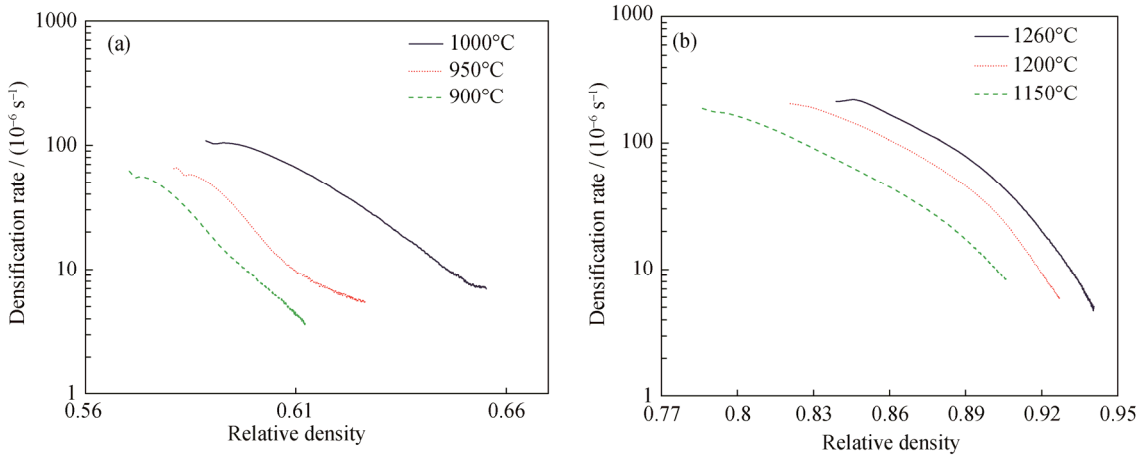

Fig. 4. Densification rate as a function of the relative density of samples with powders less than 20 µm: (a) sintered at lower temperatures and (b) for samples sintered at higher temperatures.

3.2. Activation energy

The data from Fig. 4 were used to estimate the activation energy (Q) via the equation proposed by Wang and Raj [33] based on the Arrhenius plot. Two temperature ranges were evaluated: from 900 to 1000°C and from 1150 to 1260°C. The initial Eq. (1) was proposed by Wang and Raj [33]:

$$\ln\left(T\dot{T}\frac{\mathrm{d}\rho}{\mathrm{d}T}\right)=-\frac{Q}{RT}+\ln\left[f(\rho)\right]+\ln A-n\ln G \qquad (1)$$

where $\dot{T}$ is the heating rate, G is the grain size, R is the universal gas constant, T is the absolute temperature, Q is the activation energy, $f(\rho)$ is only a function of density, n is the time exponent of sintering and A is a parameter of the material that is insensitive to G, T, and ρ.

Knowing that $\dot{T}$ is equal to the differential of the temperature with respect to time $\frac{\mathrm{d}T}{\mathrm{d}t}$ and substituting this value into Eq. (1), we obtain

$$\ln\left(T\frac{\mathrm{d}T}{\mathrm{d}t}\frac{\mathrm{d}\rho}{\mathrm{d}T}\right)=-\frac{Q}{RT}+\ln\left[f(\rho)\right]+\ln A-n\ln G \qquad (2)$$

Here, sintering is evaluated at a constant temperature, which leads to Eq. (3). This approach eliminates the differential of temperature, leaving only the change in density as a function of time:

$$\ln\left(T\frac{\mathrm{d}\rho}{\mathrm{d}t}\right)=-\frac{Q}{RT}+\ln\left[f(\rho)\right]+\ln A-n\ln G \qquad (3)$$

The terms on the right-hand side of Eq. (3) involve grain growth and are considered negligible because the particle size and relative density at which analyses were performed are not significant for grain growth. Thus, we calculated the activation energy by measuring the densification rate reached at a given relative density for different sintering temperatures (Eq. (3)).

Fig. 5(a) shows the Arrhenius plots for the samples sintered between 900 and 1000°C, and Fig. 5(b) shows those sintered between 1150 and 1260°C. To calculate the value of Q, a linear regression is performed, and the value of the slope of the points corresponds to Q/R, where the value of Q is obtained by knowing that $R = 8.314$ J·mol^{-1}·K^{-1}.

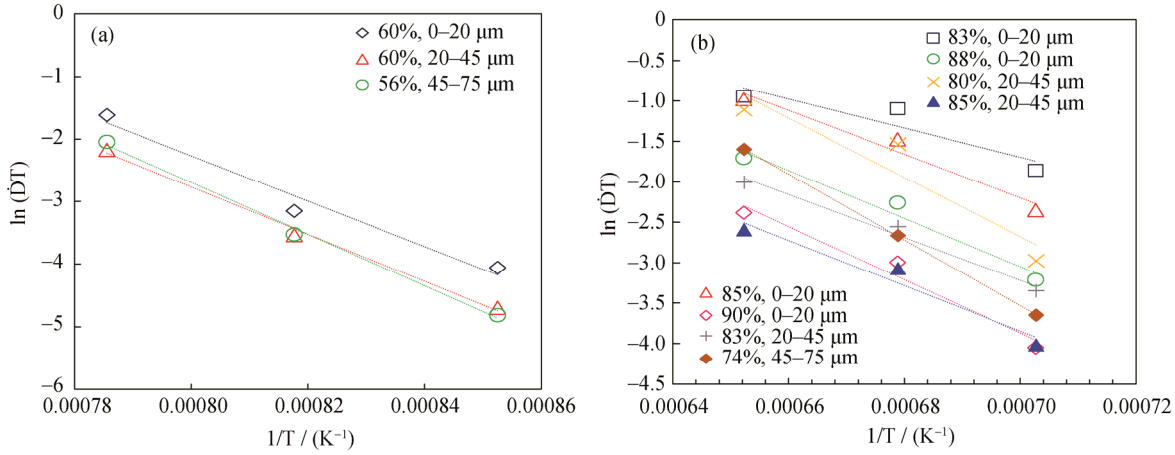

Fig. 5. Arrhenius plots of the densification rate for the estimate of activation energies: (a) lower temperatures and (b) higher temperatures.

Three values of Q were estimated at low temperatures (Table 1). The values of Q for the finest and intermediate powders at the same relative density (0.6) are quite similar: 302 ± 8 kJ·mol^{-1} and 313 kJ·mol^{-1}, respectively. The value of Q for the coarser powders was 343 ± 2 kJ·mol^{-1}, which is 12% higher than that obtained for smaller powders. Nevertheless, this value was estimated for a relative density of 0.56.

Table 1. Activation energies of the Ti6Al4V alloy calculated in the lower temperature range (900–1050°C, in which the α phase is predominant) for the different particle size distribution ranges

Temperature range	Size of particles / μm	Relative density / %	Q / (kJ·mol^{-1})
900–1050°C (α phase of Ti6Al4V alloy)	0–20	60	302 ± 8
	20–45	60	313 ± 2
	45–75	56	343 ± 2

Fig. 5(b) shows that a larger number of estimates of Q can be made from 1150 to 1260°C because more common values of relative density were found between the different particle sizes. The values of Q for the finest powders are 225, 247, and 273 kJ·mol^{-1} for relative densities from 0.85 to 0.9 (Table 2).

Table 2. Values of the activation energy of the Ti6Al4V alloy calculated in the higher temperature range, for the different particle size distribution ranges

Temperature range	Size of particles / μm	Relative density / %	Q / (kJ·mol^{-1})
1150–1260°C (β phase of Ti6Al4V alloy)	0–20	85	225 ± 5
	0–20	88	247 ± 4
	0–20	90	273 ± 5
	20–45	80	304 ± 16
	20–45	83	220 ± 1
	20–45	85	232 ± 5
	45–75	74	338 ± 1

For the intermediate powders (20–45 μm), three values of the activation energy were estimated (304, 220, and 232 kJ·mol^{-1}) at three different relative density values of 80%, 83%, and 85%, respectively. For coarser powders, only one value of Q could be estimated (338 kJ·mol^{-1} at 74% of the relative density). If the activation energy values are compared for samples with the same densification, then we find that the fine and coarse powders with 85% relatively density had practically the same values. Therefore, the activation energy is not directly affected by the particle size. Rather, an effect related to the relative density of the material was found. This effect depends on the particle size and the sintering temperature and is intrinsically related to the growth of the necks and the local configuration of the particles.

The range of estimated Q values is 225 to 343 kJ·mol^{-1} for relative densities between 56% and 90%. Different authors have reported that lattice self-diffusion is the driving mechanism for both α and β phases of the titanium, giving a range of activation energies from 123 to 328 kJ·mol^{-1} [18,31,34–39]. Robertson and Schaffer [38] also estimated the activation energy of the Ti6Al4V powders with a particle size distribution of 90–106 μm and found a value of 290 kJ·mol^{-1}; they concluding that lattice self-diffusion is the predominant mechanism. Xu and Nash [23] estimated the activation energy of Ti6Al4V powders with different relative densities and found values similar to those reported in the present work; nevertheless, they concluded that lattice self-diffusion is the predominant diffusion sintering mechanism. However, the range of values is relatively wide and it includes values of Q that could be associated with either volume or grain-boundary diffusion mechanisms. Notably, the value of Q in the present work decreases with increasing relative density; for example, Q values greater than 300 kJ·mol^{-1} are obtained for relative densities lower than 80% regardless of the sintering size or the temperature. Q values between 220 and 240 kJ·mol^{-1} are estimated for relative densities from 80% to 90%. At densities greater than 90%, Q increases to 273 kJ·mol^{-1}. This behavior reflects the different sintering stages suggested in the sintering diagrams constructed by Swinkels and Ashby [40]. This behavior also suggests that the existing local microstructure affects the ratio between the neck size and particle size, which controls the redistribution of mass during sintering.

Therefore, based on the values obtained from the activation energy, we conclude that the first stage results in a relative density as high as 80% and is controlled by the volume diffusion mechanism. The intermediate stage is then controlled by the grain-boundary diffusion mechanism. This stage ends at approximately 90% relative density. The last stage is controlled by the lattice self-diffusion mechanism. A change in the mechanism of grain-boundary diffusion in the network when the relative density reached approximately 90% was observed for sintered alumina particles with an average size of 3 μm [41]. This value was also found for 10 μm silver particles [40] and for stainless steel particles [42].

3.3. SEM analysis

The sintered samples at the highest temperature (1260°C), whose images from three different particle sizes are shown in Figs. 6(a)–6(c). Samples sintered at the lowest tempera-

ture (900°C) are presented in Figs. 6(d)–6(f) and include the three different sizes. The pore size and volume decrease as particle size decreases. Spherical and isolated pores are found in the sample with the highest relative density (96%; Fig. 6(a)). Meanwhile, the shape of the coarser particles is still evident even when sintered at the highest temperature (Fig. 6(c)).

A lamellar microstructure was detected for samples sintered above the β transition as shown in Figs. 6(a)–6(c). By contrast, samples sintered at the lowest temperature show small necks. The sample prepared from the coarser particles appears to exhibit only adhesion contact (Fig. 6(f)). The porosity of the samples is clearly affected by the sintering temperature and by the particle size of the powders, as expected.

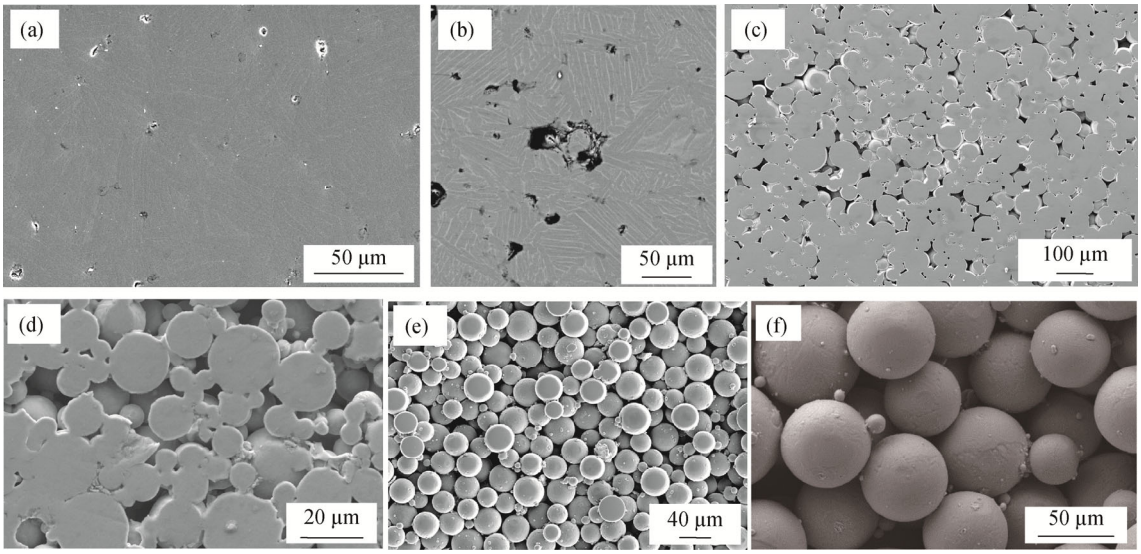

Fig. 6. SEM micrographs of samples sintered at 1260°C for (a) 0–20 μm, (b) 20–45 μm, and (c) 45–75 μm; and sintered at 900°C for (d) 0−20 μm, (e) 20–45 μm, and (f) 45–75 μm.

3.4. Mechanical properties

3.4.1. Microhardness

To assess the progression of sintering, microhardness measurements were performed with a load of 500 g on the polished surfaces. To obtain a representative value of the interparticle bonding during sintering, indentations were made at the neck sizes developed between particles. Thus, some samples were not measured because indentations could not be made between particles because the necks were too small to be indented (Figs. 6(e) and 6(f)). The average values for the microhardness as a function of temperature are shown in Fig. 7. The microhardness values increased with increasing sintering temperature for all particle sizes. The maximum microhardness value was HV 353, which is almost four times higher than the lowest value (HV 89).

The highest value is similar to that reported by Yan *et al.* [8], who determined a value of HV 354 for a sample prepared with 44-μm Ti6Al4V powder and at a sintering temperature similar to that used in the present work. The highest value is also similar to the values reported by Chávez *et al.* [30] for powders with a size distribution of less than 45 μm and sintered between 1200 and 1400°C. However, these values are slightly lower than those reported by Khan *et al.* [25] (values of HV 364 to HV 483), who sintered pre-alloyed < 20 μm powders of Ti6Al4V at 1300°C. Notably, the values obtained decreased as the particle size was increased for the same sintering temperature. This observation is explained mainly by the relative density obtained with coarser powders being lower than that obtained with the finer ones. Fig. 7(b) shows the average values of the microhardness as a function of the relative density; a linear behavior is observed, where the microhardness increases as much as the relative density. Nevertheless, microhardness values for samples with the same relative density but with different particle sizes indicate contradictory effects. For samples with lower densities, smaller particles result in higher microhardness; meanwhile, samples with relative densities of approximately 90% exhibit larger intermediate particle sizes with respect to the finest ones. This observation is possibly associated with the grain size, which likely grew during sintering for the finest particles, as evident in Figs. 6(a) and 6(b). Thus, the residual porosity exerts less influence than the grain size on the microhardness values.

3.4.2. Compression tests

The compression behavior of samples with different particle sizes and sintered at different temperatures is shown in Fig. 8. The stress–strain curves of the 20–45 μm samples

sintered at 900 to 1260°C are presented in Fig. 8(a). As expected, the compressive resistance decreases with increasing sintering temperature. This behavior is consistent with the lower relative density reached during sintering. The curve shows three stages. The first stage is a steep stress increase that corresponds to linear elastic behavior. In the second stage, the stress gently increases, suggesting plastic deformation. The final stage shows a decrease in stress, indicating sample failure.

Next, to evaluate the effect of particle size and initial packing, the stress–strain curves for samples with different particles sizes sintered at 1260°C and prepared from uniaxial compression and loose powders are shown in Fig. 8(b). The compression resistance decreased with increasing particle size. This trend is logical because the relative density decreased as well. Fig. 8(b) shows that porosity plays a major role in the compression properties rather than the particle size of the powders or the initial packing of the samples. The pore volume fraction remaining after sintering does not increase the strain of the samples, unlike samples with artificially large pores [28,43].

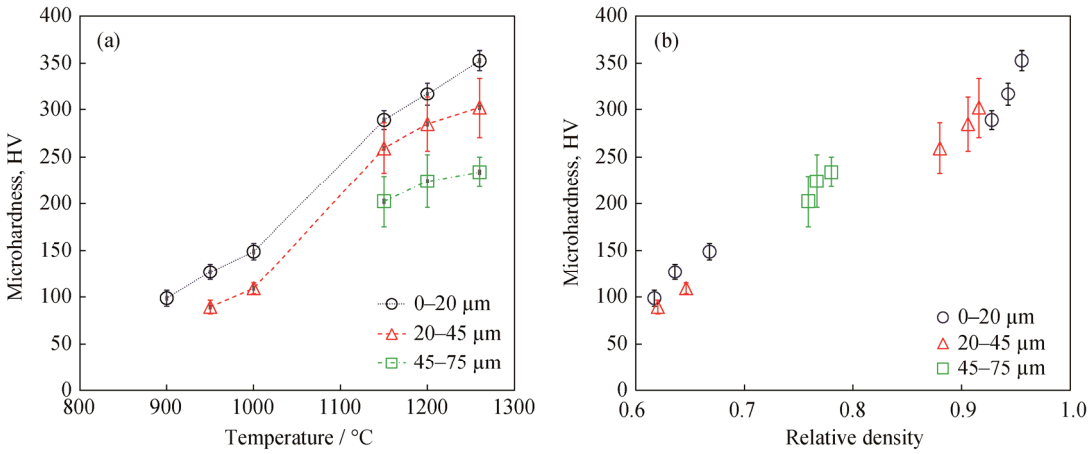

Fig. 7. Average values of microhardness for the different particle size ranges as a function of (a) the sintering temperature and (b) the relative density.

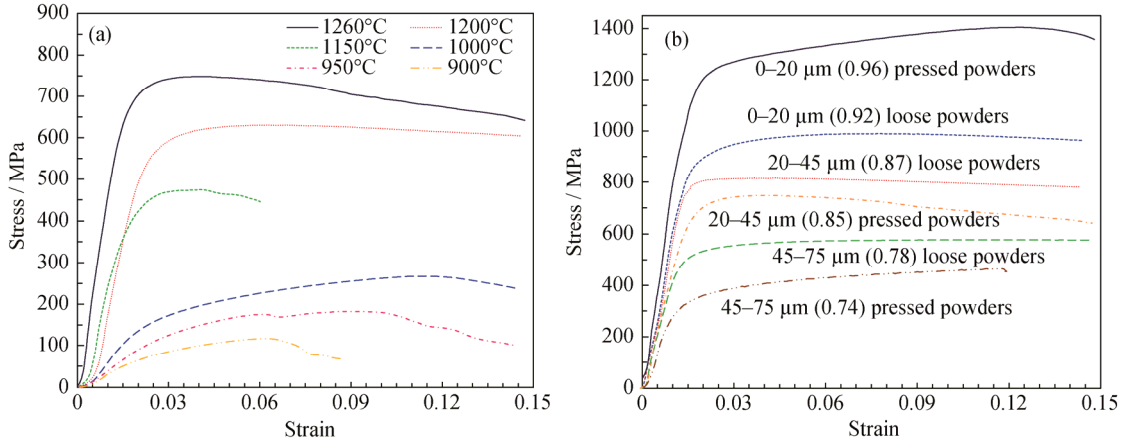

Fig. 8. True stress–strain compression curves (a) for samples sintered at different temperatures and composed of powders between 20 and 45 μm and (b) for samples with different particle sizes and sintered at 1260°C.

To establish the effect of particle size on mechanical strength, values of E and the yield strength (σ_{yield}) were estimated from the stress–strain curves. Because the mechanical strength strongly depends on the porosity, values of E and σ_{yield} are plotted as functions of the relative density in Fig. 9.

Both the E and the σ_{yield} exhibit polynomial behavior as a function of relative density regardless of the particle size and the sintering temperature. A wide range of E values were obtained (3 to 85 GPa; Fig. 9(a)). A 10% pore volume fraction can reduce the theoretical E value for the casting alloy by up to 50%. This effect is slightly lower for σ_{yield}, where a 15% porosity is required to reduce the yield stress to 50%. The range of values for the σ_{yield} is from 50 to 800 MPa (Fig. 9(b)). A comparison of the E of samples with approximately the same relative density but prepared with dif-

ferent particle sizes reveals that the E values are very similar except when samples with 75% relative density were prepared with particles < 20 μm and 45–75 μm. The samples with the coarser powders have an E value twice as high as that of the finest particles. This difference in E values could arise from the difference in sintering temperatures used to achieve the same relative density. Coarser powders were sintered at 1260°C, whereas the finest powers were sintered at 1000°C. The sintering temperature likely affects the size of the interparticle necks developed during sintering, which results in greater sample elasticity. However, the σ_{yield} is unaffected by particle size.

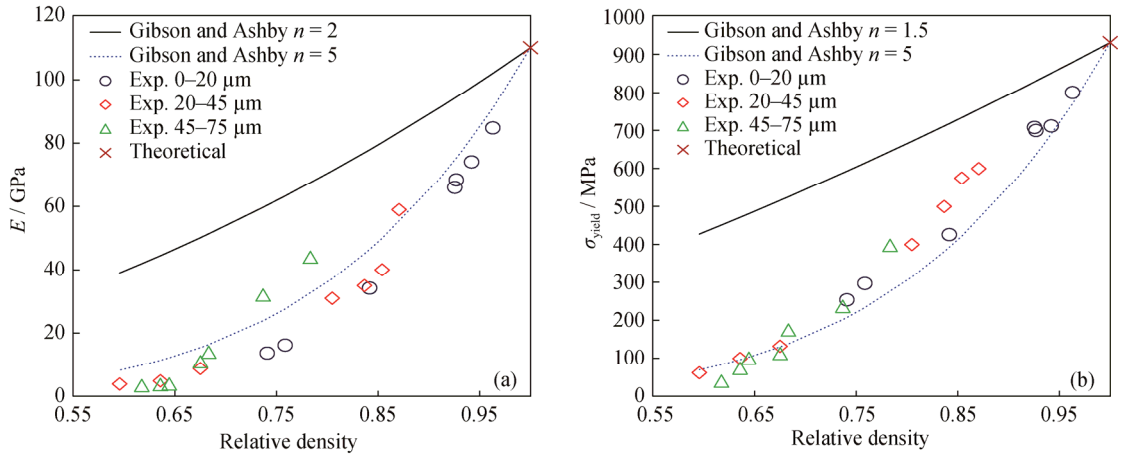

Fig. 9. Mechanical properties of the sintered samples as a function of the relative density: (a) Young's modulus and (b) yield stress.

The results were compared to several models proposed in the literature for both E [44–47] and σ_{yield} [46–48] (Table 3). Most of the models are based on the Gibson and Ashby power law [46] with some changes to parameters related to the pore shape, critical pore volume fraction, etc. However, these parameters are not easy to assess and most of them only work for the system proposed by each author. Thus, we used a straight line to compare the experimental results with the power law proposed by Gibson and Ashby (Fig. 9). The values obtained from the model overestimate the experimental ones; nevertheless, the behavior proposed by the power law is pertinent. Therefore, the exponent n in the power law was fitted for the experimental E values, and n = 5 was found to give a good match with the experimental values (Fig. 9(a)). The same value of n was used to estimate the σ_{yield}, resulting in good agreement with the experimental results.

3.4.3. Fracture analysis

Fracture micrographs after compression testing of samples with different relative densities are shown in Fig. 10. The images are ordered according to the relative density of the samples from 58% to 96%. Figs. 10(a)–10(c) shows samples with a relative density lower than 88%. Failure clearly occurred at the interparticle necks, indicating the concentration of stress in this area. However, samples with a relative density of 92% show failure at both interparticle necks and inside the particles (Fig. 10(d)) [49–51]. This observation indicates that the resistance reached this degree of densification to facilitate a more continuous matrix. Thus, the porosity begins to be more isolated and failure can therefore occur anywhere.

Table 3. Models proposed to predict the behavior of E and σ_{yield} as functions of relative density

Model	Constant values	Authors
$E = E_0\left(1-\frac{p}{a}\right)^n$	$a = 0.45$ $n = 1.64$	Kovacik [44–45]
$E = E_0 D^n$	$n = 2$	Gibson and Ashby [46]
$E = E_0 a(1-p)^n$	$a = 1.018$ $n = 2.707$	Simoneau *et al.* [47]
$\sigma = \sigma_0\left(\frac{D}{D_0}\right)^n$	$n = 1.5$	Gibson and Ashby [46]
$E = E_0\left[\frac{(1-p)^2}{1+\left(\frac{1}{F_f}-1\right)p}\right]$	$F_f = 4pA/PE^2$	Nielsen [48]

The sample with a density of 94% (Fig. 10(e)) shows that the failure originated in the isolated pores, indicating a stress concentrator. Finally, the sample with the highest density (96%; Fig. 10(f)) exhibits failure at the intergranular level. The sample is preferentially broken through the grain boundaries or through the division of the lamellar microstructure

obtained from sintering this type of powder. This breakage occur parallel to sheets of the β phase, which are the weakest of the alloy. The type of fracture found in samples with densification greater than 92% is associated with isolated pores that are nearly spherical, as reported for forged titanium alloys [52].

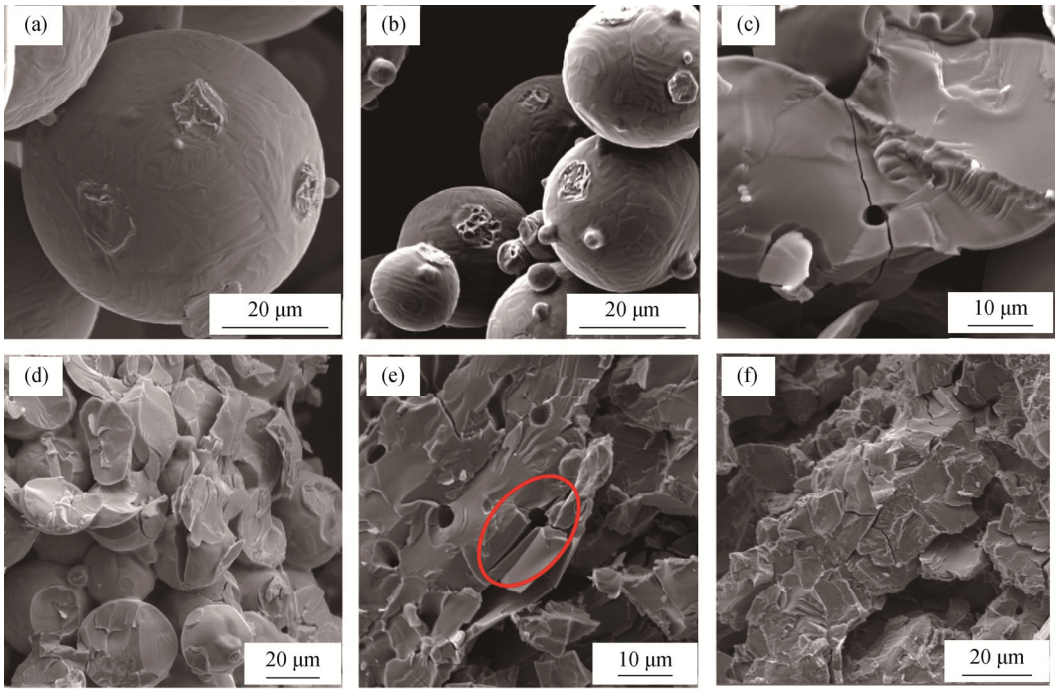

Fig. 10. SEM micrographs of samples with different relative densities, after the samples were subjected to compression tests: (a) 58%, (b) 62%, (c) 88%, (d) 92%, (e) 94%, and (f) 96%, respectively.

This analysis suggests that the type of rupture generated during compression tests is a function of the neck size between particles, which is closely linked to the relative density in the sample. Thus, sintering geometry shows that the ratio between shrinkage ($\Delta L/L_0$) and neck ratio (X/D) is [49]

$$\left(\frac{X}{D}\right)=\left(\frac{\Delta L}{L_0}b\right)^{1/2} \tag{4}$$

where X/D is the ratio of the diameter of the neck (X) to the diameter of the particle (D), $\Delta L/L_0$ is the sample shrinkage, and b is a parameter determined experimentally (b = 3.6 in this work).

Similarly, the usual assumption is that volume changes during sintering ($\Delta V/V_0$) are isotropic. Thus, if the mass remains constant during sintering, then the relative density depends on the initial green density, and the shrinkage is as follows [49]:

$$D=\frac{D_0}{\left(1+\frac{\Delta L}{L_0}\right)^3} \tag{5}$$

where D_0 is the initial relative density or green value and D is the relative density value reached.

Thus, an estimate of the relative density values as a function of the neck size and particle diameter ratio can be obtained from Eqs. (4) and (5), respectively. The neck values were measured for different samples from scanning electronic microscopy (SEM) images; the average value of 50 necks was measured, and the particle size was considered constant during the sintering process. To measure the interparticle necks, we obtained the Ferret diameter from the fracture images. For the case where the relative density of the samples is greater than 90%, the neck sizes were obtained by measuring between spherical pores, which induces a small error for samples with a relative density value greater than 90%, where grain growth may be important. However, the error can be considered smaller due to the particle size used here.

Fig. 11 shows the relative density as a function of the neck/particle size ratio estimated from Eqs. (4) and (5) as well as the experimental values obtained from the fractured samples. The values estimated from Eqs. (4) and (5) nicely approximate the experimental results.

As shown in Fig. 10, the type of fracture that occurs in samples with a densification of approximately 92% can be observed in both particles and interparticular necks, implying a change in the fracture mechanism. Given the value of

the relative density in Fig. 11, we estimate that the failure will occur at the interparticle necks when $X/D < 0.54$. Meanwhile, $X/D > 0.54$ will result in intergranular fractures. This analysis indicates that porosity rather than particle sizes or sintering conditions plays a major role in the mechanical properties of sintered materials.

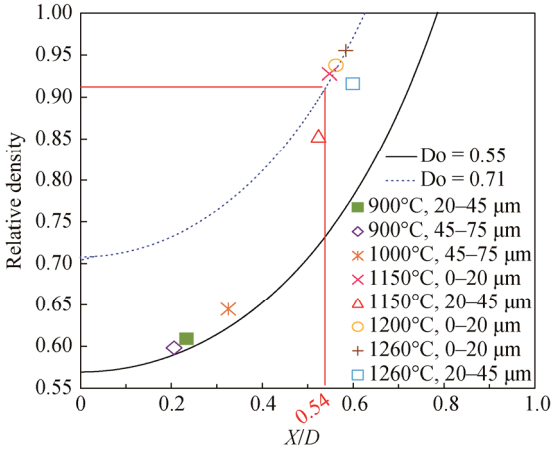

Fig. 11. Relative density as a function of the ratio of neck diameter to particle diameter.

4. Conclusions

The sintering of the samples prepared with different particle size distributions was investigated to evaluate the effect of particle size on the sintering kinetics and mechanical properties of sintered compacts. We drew the following conclusions:

As expected, the densification of samples was dependent on the particle size and sintering temperature as well as the initial packing. Densification was higher for smaller particles and higher temperatures. However, the particle size did not affect the diffusion mechanisms. Rather, the porosity evolution was assessed during sintering (or densification). This porosity evolution drives the predominant diffusion mechanisms, and they change as a function of the relative density. Volume diffusion is predominant at relative densities below 0.8. Grain-boundary diffusion drives the mass transport at relative densities from 0.8 to 0.9, and the volume diffusion is again predominant at relative densities greater than 0.9.

Compression strength was also strongly affected by the pore volume fraction; however, the particle size and sintering conditions did not affect its behavior. This behavior can be predicted by the power law proposed by Gibson and Ashby, with the exponent fitted from the experimental results.

The microhardness exhibits linear behavior with respect to the relative density; nonetheless, samples with relative densities greater than 90% were affected by the grain growth and higher values of microhardness were found for intermediate particle sizes. The fracture mechanisms are linked to the ratio between the neck and particle size, which is closely related to the relative density or pore volume fraction. In addition, the shape and interconnectivity of the porosity plays a major role in the fracture mechanisms during compression tests. Therefore, the fracture changes from the interparticle necks to the intergranular space is estimated at an X/D ratio of approximately 0.54 when the pores become isolated. We concluded that particle size and sintering conditions affect the densification, whereas the diffusion mechanisms, compression properties, and fracture mechanisms were not affected.

Acknowledgements

The authors would like to thank to Coordination of Scientific Research of the University Michoacana of San Nicolás of Hidalgo (UMSNH), the National Laboratory SEDEAM-National Council for Science and Technology (CONACYT) and ECOS M15P01 for the financial support and the facilities to develop this study.

References

[1] C. Leyens and M. Peters, *Titanium and Titanium Alloys: Fundamentals and Applications*, Wiley-VCH, Weinheim, 2003, p. 1.

[2] I. Montealegre-Meléndez, E. Neubauer, and H. Danninger, Effect of starting powder grade on sintering and properties of PM titanium metal matrix composites, *Powder Metall.*, 52(2009), No. 4, p. 322.

[3] E. Benavente-Martínez, F. Devesa, and V. Amigó, Caracterización mecánica de aleaciones Ti–Nb mediante ensayos de flexión biaxial, *Rev. Metal.*, 46(2010), p. 19.

[4] D. Banerjee and J.C. Williams, Perspectives on titanium science and technology, *Acta Mater.*, 61(2013), No. 3, p. 844.

[5] L. Reig, V. Amigó, D.J. Busquets, and J.A. Calero, Development of porous Ti6Al4V samples by microsphere sintering, *J. Mater. Process. Technol.*, 212(2012), No. 1, p. 3.

[6] D.M. Brunette, P. Tengvall, M. Textor, and P. Thomsen, *Titanium in Medicine: Material Science, Surface Science, Engineering, Biological Responses and Medical Applications*, Springer Science and Business Media, New York, 2013, p. 1.

[7] M. Yan and P. Yu, *An Overview of Densification, Microstructure and Mechanical Property of Additively Manufactured Ti–6Al–4V — Comparison Among Selective Laser Melting, Electron Beam Melting, Laser Metal Ddeposition and Selective Laser Sintering, and with Conventional Powd-*

er, Sintering Techniques of Materials, InTech, London, 2015, p. 77.

[8] Z.Q. Yan, F. Chen, Y.X. Cai, and Y.N. Jian, Influence of particle size on property of Ti–6Al–4V alloy prepared by high-velocity compaction, *Trans. Nonferrous Met. Soc. China*, 23(2013), No. 2, p. 361.

[9] Y.J. Yan, G.L. Nash, and P. Nash, Effect of density and pore morphology on fatigue properties of sintered Ti–6Al–4V, *Int. J. Fatigue*, 55(2013), p. 81.

[10] H.P. Ng, C. Haase, R. Lapovok, and Y. Estrin, Improving sinterability of Ti–6Al–4V from blended elemental powders through equal channel angular pressing, *Mater. Sci. Eng. A*, 565(2013), p. 396.

[11] Y. Torres, J.A. Rodríguez, S. Arias, M. Echeverry, S. Robledo, V. Amigo, and J.J. Pavón, Processing, characterization and biological testing of porous titanium obtained by space-holder technique, *J. Mater. Sci.*, 47(2012), No. 18, p. 6565.

[12] L. Yan, H.Y. Zhang, T. Wang, X.L. Huang, Y.Y. Li, J.S. Wu, and H.B. Chen, High-strength Ti–6Al–4V with ultrafine-grained structure fabricated by high energy ball milling and spark plasma sintering, *Mater. Sci. Eng. A*, 585(2013), p. 408.

[13] L. Xu, R.P. Guo, C.G. Bai, J.F. Lei, and R. Yang, Effect of isostatic pressing conditions and cooling rate on microstructure and properties of Ti–6Al–4V alloy from atomized powder, *J. Mater. Sci. Technol.*, 30(2014), No. 12, p. 1289.

[14] V. Amigó, M.D. Salvador, F. Romero, C. Solves, and J.F. Moreno, Microestructural evolution of Ti–6Al–4V during the sintering of microspheres of Ti for orthopedic implants, *J. Mater. Process. Technol.*, 141(2003), No. 1, p. 117.

[15] L.E. Murr, E.V. Esquivel, S.A. Quinones, S.M. Gaytan, M.I. Lopez, E.Y. Martinez, F. Medina, D.H. Hernandez, E. Martinez, J.L. Martinez, S.W. Stafford, D.K. Brown, T. Hoppe, W. Meyers, U. Lindhe, and R.B. Wicker, Microstructures and mechanical properties of electron beam-rapid manufactured Ti–6Al–4V biomedical prototypes compared to wrought Ti–6Al–4V, *Mater. Charact.*, 60(2009), No. 2, p. 96.

[16] N.W. Hrabe, P. Heinl, B. Flinn, C. Körner, and R.K. Bordia, Compression-compression fatigue of selective electron beam melted cellular titanium (Ti–6Al–4V), *J. Biomed. Mater. Res. Part B*, 99(2011), No. 2, p. 313.

[17] L. Bolzoni, T. Weissgaerber, B. Kieback, E.M. Ruiz-Navas, and E. Gordo, Mechanical behavior of pressed and sintered CP Ti and Ti–6Al–7Nb alloy obtained from master alloy addition powder, *J. Mech. Behav. Biomed. Mater.*, 20(2013), p. 149.

[18] R.M. German, *Sintering Theory and Practice*, John Wiley and Sons, New York, USA, 1996, p. 100.

[19] H. Bayat, M. Rastgo, M.M. Zadeh, and H. Vereecken, Particle size distribution models, their characteristics and fitting capability, *J. Hydrol.*, 529(2015), p. 872.

[20] S.S. Razavi-Tousi, R. Yazdani-Rad, and S.A. Manafi, Effect of volume fraction and particle size of alumina reinforcement on compaction and densification behavior of Al–Al_2O_3 nanocomposites, *Mater. Sci. Eng. A*, 528(2011), No. 3, p. 1105.

[21] W. Chen, Y. Yamamoto, W.H. Peter, M.B. Clark, S.D. Nunn, J.O. Kiggans, T.R. Muth, C.A. Blue, J.C. Williams, and K. Akhtar, The investigation of die-pressing and sintering behavior of ITP CP-Ti and Ti–6Al–4V powders, *J. Alloys Compd.*, 541(2012), p. 440.

[22] R. Lapovok, D. Tomus, and B.C. Muddle, Low-temperature compaction of Ti–6Al–4V powder equal channel angular extrusion with back pressure, *Mater. Sci. Eng. A*, 490(2008), No. 1-2, p. 171.

[23] X.Y. Xu and P. Nash, Sintering mechanisms of Armstrong prealloyed Ti–6Al–4V powders, *Mater. Sci. Eng. A*, 607(2014), p. 409.

[24] O.M. Ivasishin, D.G. Savvakin, F. Froes, V.C. Mokson, and K.A. Bondareva, Synthesis of alloy Ti–6Al–4V with low residual porosity by a powder metallurgy method, *Powder Metall. Met. Ceram.*, 41(2002), No. 7-8, p. 382.

[25] D.F. Khan, H.Q. Yin, H. Li, X.H. Qu, M. Khan, S. Ali, and M.Z. Iqbal, Compaction of Ti–6Al–4V powder using high velocity compaction technique, *Mater. Des.*, 50(2013), p. 479.

[26] M. P. I. Federation, *Standard Test Methods for Metal Powders and Powder Metallurgy Products*, Metal Powder Industries Federation, Princeton, 2002, p. 1.

[27] M. Dewidar, Microstructure and mechanical properties of biocompatible high density Ti–6Al–4V/W produced by high frequency induction heating sintering, *Mater. Des.*, 31(2010), No. 8, p. 3964.

[28] X.Y. Cheng, S.J. Li, L.E. Murr, Z.B. Zhang, Y.L. Hao, R. Yang, F. Medina, and R.B. Wicker, Compression deformation behavior of Ti–6Al–4V alloy with cellular structures fabricated by electron beam melting, *J. Mech. Behav. Biomed. Mater.*, 16(2012), p. 153.

[29] L. Bolzoni, E.M. Ruiz-Navas, and E. Gordo. Feasibility study of the production of biomedical Ti–6Al–4V alloy by powder metallurgy, *Mater. Sci. Eng. C*, 49(2015), p. 400.

[30] J. Chávez, L. Olmos, O. Jiménez, D. Bouvard, E. Rodríguez, and M. Florers, Sintering behaviour and mechanical characterisation of Ti64/*x*TiN composites and bilayer components, *Powder Metall.*, 60(2017), No. 4, p. 257.

[31] B.B. Panigrahi, M.M. Godkhindi, K. Das, P.G. Mukunda, and P. Ramakrishnan, Sintering kinetics of micrometric titanium powder, *Mater. Sci. Eng. A*, 396(2005), No. 1-2, p. 255.

[32] Y. Kim, Y.B. Song, S.H. Lee, and Y.S. Kwon, Characterization of the hot deformation behavior and microstructural evolution of Ti–6Al–4V sintered performs using materials modeling techniques, *J. Alloys Compd.*, 676(2016), p. 15.

[33] J. Wang and R. Raj, Estimate of the activation energies for boundary diffusion from rate-controlled sintering of pure alumina, and alumina doped with zirconia or Titania, *J. Am. Ceram. Soc.*, 73(1990), No. 5, p. 1172.

[34] Y. Mishin and C. Herzig, Diffusion in the Ti–Al system, *Acta Mater.*, 48(2000), No. 3, p. 589.

[35] A.E. Pontau and D. Lazarus, Diffusion of titanium and niobium in bcc Ti–Nb alloys, *Phys. Rev. B: Condens. Matter*,

19(1979), No. 8, p. 4027.

[36] M. Köppers, C. Herzig, M. Friesel, and Y. Mishin, Intrinsic self-diffusion and substitutional Al diffusion in α-Ti, *Acta Mater.*, 45(1997), No. 10, p. 4181.

[37] G. Neumann, V. Tölle, and C. Tuijn, On the impurity diffusion in β-Ti, *Physica B*, 296(2001), No. 4, p. 334.

[38] I.M. Robertson and G.B. Schaffer, Some effects of particle size on the sintering of titanium and a master sintering curve model, *Metall. Mater. Trans. A*, 40(2009), No. 8, p. 1968.

[39] C. Herzig, T. Wilger, T. Przeorski, F. Hisker, and S. Divinski, Titanium tracer diffusion in grain boundaries of α-Ti, α_2-Ti_3Al, and γ-TiAl and in α_2/γ interphase boundaries, *Intermetallics*, 9(2001), No. 5, p. 431.

[40] F.B. Swinkels and M.F. Ashby, A second report on sintering diagrams, *Acta Metal.*, 29(1981), No. 2, p. 259.

[41] S.J.L. Kang and Y.I. Jung, Sintering kinetics at final stage sintering: model calculation and map construction, *Acta Mater.*, 52(2004), No. 15, p. 4573.

[42] R.M. German, The sintering of 304L stainless steel powder. *Metall. Trans. A*, 7(1976), No. 12, p. 1879.

[43] Y. Torres, S. Lascano, J. Bris, J. Pavón, and J.A. Rodriguez, Development of porous titanium for biomedical applications: A comparison between loose sintering and space-holder techniques, *Mater. Sci. Eng. C*, 37(2014), p. 148.

[44] J. Kováčik, The tensile behavior of porous metals made by GASAR process, *Acta Mater.*, 46(1998), No. 15, p. 5413.

[45] J. Kováčik, Correlation between Young's modulus and porosity in porous materials, *J. Mater. Sci. Lett.*, 18(1999), No. 13, p. 1007.

[46] L.J. Gibson and M.F. Ashby, *Cellular Solids: Structure and Properties*, Cambridge University Press, Cambridge, 1999, p. 52.

[47] C. Simoneau, V. Brailovski, and P. Terriault, Design, manufacture and tensile properties of stochastic porous metallic structures, *Mech. Mater.*, 94(2016), p. 26.

[48] L.F. Nielsen, Elasticity and damping of porous materials and impregnated materials, *J. Am. Ceram. Soc.*, 67(1984), No. 2, p. 93.

[49] R.M. German, *Sintering: From Empirical Observations to Scientific Principles*, Butterworth-Heinemann Elsevier Ltd, Oxford, 2014, p. 141.

[50] A. Taşdemirci, A. Hızal, M. Altındiş, I.W. Hall, and M. Gü den, The effect of strain rate on the compressive deformation behavior of a sintered Ti6Al4V powder compact, *Mater. Sci. Eng. A*, 474(2008), No. 1-2, p. 335.

[51] M.E. Dizlek, M. Guden, U. Turkan, and A. Tasdemirci, Processing compression testing of Ti6Al4V foams for biomedical applications, *J. Mater. Sci.*, 44(2009), No. 6, p. 1512.

[52] D. Eylon, F.H. Froes, D.G. Heggie, P.A. Blenkinsop, and R.W. Gardiner, Influence of thermomechanical processing on low cycle fatigue of prealloyed Ti–6Al–4V powder compacts, *Metall. Trans. A*, 14(1983), No. 12, p. 2497.